IEEE Open Journal of the
Industrial Electronics Society

Received 7 March 2026; accepted 16 April 2026. Date of publication 21 April 2026;
date of current version 6 May 2026. The review of this article was arranged by Associate Editor Francisco D. Freijedo.

Digital Object Identifier 10.1109/OJIES.2026.3686030

Medium-Frequency Transformer for SST Applications: Design and Optimization

REZA MIRZADARANI (Graduate Student Member, IEEE), LEONARDO BOLZONELLA (Student Member, IEEE), ZHENGZHAO LI (Student Member, IEEE), ZIAN QIN (Senior Member, IEEE), PETER VAESSEN (Member, IEEE), PAVOL BAUER (Senior Member, IEEE), AND MOHAMAD GHAFFARIAN NIASAR (Member, IEEE)

Department of Electrical Sustainable Energy, Delft University of Technology, 2628, CD Delft, The Netherlands

CORRESPONDING AUTHOR: MOHAMAD GHAFFARIAN NIASAR (e-mail: M.Ghaffarianniasar@tudelft.nl).

This work was supported by the RVO MOOI (Missiegedreven Onderzoek Ontwikkeling en Innovatie) under Grant MOOI 52103.

ABSTRACT This work presents a downscaled validation of a medium-voltage, medium-frequency transformer (MFT) concept designed for high-current operation on the secondary side using multiple parallel paths. The design is based on a modular winding approach, which simplifies the construction process and conductor placement on the bobbin. A systematic design and optimization procedure is developed, combining analytical calculations and finite-element simulations to explore the mass–efficiency tradeoff and to select a candidate design that meets specified leakage inductance and loss targets. The developed prototype serves as a proof of concept, demonstrating that the electrical, magnetic, and insulation requirements of the full-scale MFT can be effectively verified at reduced power levels. The fabricated prototype is tested under short-circuit and partial discharge conditions. The impedance measurements confirmed the expected resonance behavior, and the partial discharge test results verified sufficient insulation performance under high-voltage stress. The results provide experimental evidence for the scalability and feasibility of the proposed transformer design and offer guidelines for the use of 3D-printed supports, grain-oriented electrical steel cores, and windings in medium-voltage, MFT systems for hydrogen production applications.

INDEX TERMS Hydrogen production power systems, medium-frequency transformer (MFT), partial discharge (PD) testing, solid-state transformer (SST).

I. INTRODUCTION

The increasing demand for renewable energy integration and large-scale electrification requires power conversion systems that are efficient, compact, and reliable. In particular, green hydrogen production relies on electrolyzers that operate at relatively low dc voltages but require power to be delivered from medium-voltage grids at multimegawatt levels [1], [2], [3], [4]. Traditional solutions based on 50/60 Hz transformers and rectifiers are technically mature but often result in bulky systems with limited flexibility. These limitations become critical when space, efficiency, and controllability are important design factors.

In conventional installations, 50/60 Hz transformers are used to step down the grid voltage, and 6-, 12-, or 24-pulse rectifiers convert AC to DC for the electrolyzers. Although these architectures are robust, their size and weight increase significantly with rating, and they offer limited possibilities for advanced control of power flow and power quality. As green hydrogen facilities move toward tens of megawatts and are increasingly connected to medium-voltage grids or HVDC-based offshore wind systems, these constraints motivate the use of alternative power conversion concepts that can provide galvanic isolation, voltage transformation, and power conditioning in a more compact form.

Solid-state transformers (SSTs) have emerged as a promising alternative for such applications [5]. By combining power electronic converters (PECs) with a medium-frequency transformer (MFT), SSTs provide voltage scaling, galvanic isolation, and enhanced controllability in a more compact form [6], [7], [8], [9], [10]. Operation at higher frequencies allows for

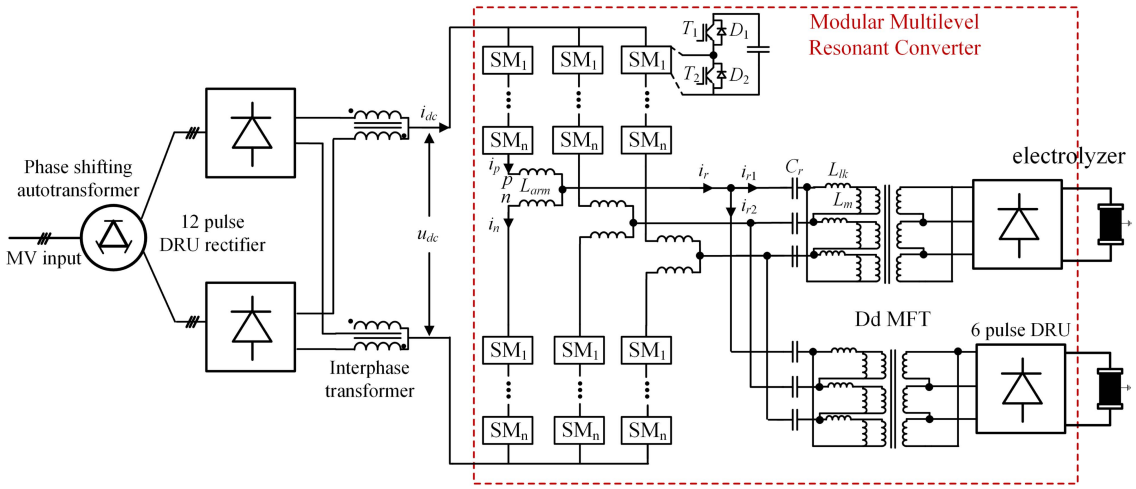

FIGURE 1. Full-scale system based on a modular multilevel resonant (MMR) converter feeding electrolyzers. The system includes a phase-shifting autotransformer, 12-pulse DRU with interphase transformer, modular multilevel arms with SM, MFT, and output rectifiers.

TABLE 1. Survey of MFTs With Corresponding Electrical, Structural, and Insulation Parameters

Title	P (kVA)	f (kHz)	Cooling	Insulation	Voltage (kV)	Insulation Tests
Virginia Tech [12]	15	500	Natural convection	Solid	4.16	30 kV BIL test, 12 kV AC applied voltage, Partial discharge $\leq$ 3.8 pC
EPFL [13]	100	10	Natural convection	Air	0.75	4 kV partial discharge
RWTH [14]	200	1.55	NA	Solid	25	±25 kV dielectric strength test
Chalmers [15]	50	5	Oil	Oil	4.5	125 kV DC test voltage
Texas [16]	200	15	Natural convection	Solid	NA	Tested at 12 kV AC peak, PD-free up to 5.3 kV rms
Wisconsin [17]	100	50	Conduction	Solid	4.16	30 kV BIL test
Tsinghua [18]	60	10	NA	Solid	10	Partial discharge test at 10 kV, applied voltage test at 20 kV
GIT [19]	50	16	Forced air	Solid	7.2	55 kV BIL, 60 kV Hipot, 90 kV lightning impulse
SPEC [20]	3000	60	Forced air	Solid	13.8	60 kV Lightning Impulse Test, 34 kV Applied Voltage Test, 23.5 kV Partial Discharge Test
NCSU [21]	100	20	Oil	Oil	7.2	10 kV DC Hipot Test, 20 kV Bushing Clearance Test
Huawei [22]	28.4	40	Forced air	Solid	12	34 kV RMS applied voltage, 75 kV lightning impulse test, Partial discharge $\leq$ 10 pC
Virginia Tech [23]	15	200	Forced air	Solid	4.16	30 kV BIL, 12 kVrms Withstand, 5.4 kVrms Partial Discharge Test
Wuhan University [24]	1000	10	NA	Solid	10	NA
Zhejiang University [25]	20	50	NA	Solid	0.75	15 kV RMS line-frequency applied voltage
SPEC [6]	1000	10	NA	Solid	10	NA
Virginia Tech [26]	15	180	NA	Solid	1.6	29 kV insulation capability
FREEDM [7]	1000	10	NA	Solid	13.2	Partial Discharge (PD) tests per IEC 60076-11, max PD level 10 pC
Present study	30×2	1	Natural convection	Solid	2.54	Standard-compliant (IEC 60076-11/60270); applied-voltage tests beyond requirement (20 kV vs. 10 kV). Breakdown at 20/17.5 kV and PD $<$ 2.5 pC under resonant excitation, confirming MV dry-type feasibility.

significantly reduced transformer size and weight. Several SST topologies have been proposed, and ongoing research focuses on optimizing transformer design, insulation systems, and thermal management to ensure reliable operation in demanding medium-voltage environments, such as hydrogen production facilities [7], [11].

Recent works on SSTs for green hydrogen production have considered different converter structures, including dual active bridge (DAB), cascaded input-series output-parallel (ISOP), modular multilevel converter (MMC), and resonant modular multilevel resonant converter (MMR) topologies [3]. For large-scale electrolyzer systems in the 10–50 MW range, three-phase SSTs with MFTs are generally preferred over single-phase solutions, due to better utilization of the magnetic core, reduced current stress in the windings, and improved harmonic performance [2]. In this context, MMR-based SSTs offer a favorable tradeoff between efficiency, converter complexity, and transformer rating, since the resonant currents enable soft switching and reduce switching losses at medium frequencies, as shown in Fig. 1 [3].

To position the proposed design relative to the state of the art, recent medium-voltage MFT studies are summarized in Table 1. The comparison focuses on electrical ratings, insulation concepts, and reported insulation validation procedures. In contrast to many existing works that primarily report analytical or limited dielectric testing, the present study includes standard-compliant applied-voltage and partial discharge (PD) measurements performed under resonant operating conditions.

The implementation of medium-voltage, MFTs in SSTs introduces several design challenges. Compared with 50/60 Hz transformers, MFTs must operate at higher frequencies,

TABLE 2. Comparison Between Full-Scale and Prototype Systems

Parameter	Full-Scale	Prototype
Number of phases	3	3
Power	2×22.5 MVA	2×30 kVA
V_{in}	25.5 kV	2.45 kV
V_{out}	650 V	65 V
N_p	60	231
N_s	2	5
Main frequency	1 kHz	1 kHz
Cooling	Oil	Natural air
Insulation	Oil-immersed paper	Dry

while satisfying insulation coordination, losses, and thermal constraints under nonsinusoidal excitation. Conventional standards, such as IEC 60076 [27], IEC 60270 [28], and IEEE 519 [29], are formulated primarily for 50/60 Hz transformers and grid-connected equipment, and their direct application to MFTs can lead to overdimensioned designs or insufficiently specified test conditions. Therefore, there is a need for practical design and validation procedures that adapt these standards to medium-frequency operation and link transformer-level performance to system-level requirements in SSTs.

Another important aspect is the design of high-current secondary windings and their interfaces with PECs. For electrolyzer applications, the DC output must be delivered at relatively low voltage but high current, which often requires multiple parallel paths in the transformer secondary to limit current density and conduction losses. The resulting winding structures are sensitive to current unbalancing, leakage inductance, and local electric field enhancement. Design choices, such as the number of parallel paths, conductor geometry, and spatial arrangement within the window, have a direct impact on losses, leakage inductance, and insulation margins, and must be verified by a combination of analytical calculations and finite-element (FEM) simulations [30].

Prototype-level validation is a key step to bridge the gap between analytical design and full-scale industrial implementation [31]. Testing at full medium voltage and power is costly and complex, especially at kilohertz frequencies. Downscaled transformers that preserve relevant electrical, magnetic, and insulation characteristics provide a practical route to verify design assumptions, evaluate manufacturing procedures, and refine test methods before constructing a full-scale MFT. Such prototypes should reproduce the main design features, including modular winding structures, insulation distances, and core materials, while operating at representative frequencies and flux densities. The full-scale and prototype systems of the present study are summarized in Table 2.

The analytical design and optimization methods applied in this work are based on established approaches and are not intended to be novel in isolation. The contribution of this article lies in the application-oriented integration of these methods for a medium-voltage, MFT within an SST context. In particular, this article provides practical insights into the winding architecture for simultaneous high-voltage and high-current operation, the physical winding arrangement and manufacturability, and an experimentally validated downscaled testing approach, including PD measurements, to assess insulation behavior at medium frequency.

The developed prototype serves as a proof of concept, demonstrating that the electrical, magnetic, and insulation requirements of the full-scale MFT can be effectively verified at reduced power levels. Short-circuit tests at 1 kHz are performed to evaluate the impedance and loss behavior, and FEM simulations are used to analyze magnetic flux density and electric field distributions in the core, windings, and 3D-printed bobbins. PD measurements at 50 Hz are carried out according to IEC 60270 to confirm that the prototype satisfies insulation performance targets under overvoltage conditions. The proposed design and test methodology are consistent with established industry practices, including IEC 60076 for transformer design and testing.

Compared with earlier works on full-scale SST system design for electrolyzer applications, this article focuses on the detailed design, optimization, and experimental verification of a downscaled MFT prototype that implements the selected winding and core concept in a practical hardware demonstrator. The results provide experimental evidence for the scalability and feasibility of the proposed transformer design and offer guidelines for the use of modular windings, 3D-printed supports, and grain-oriented electrical steel (GOES) cores in medium-frequency, medium-voltage transformers for SST systems.

In this study, the prototype is intentionally downscaled and adopts simplified cooling and insulation approaches compared to a full-scale medium-voltage implementation. As summarized in Table 1, the prototype operates with air cooling and dry insulation, whereas the full-scale design is based on oil-immersed insulation and liquid cooling. Consequently, the presented prototype is not intended to represent a directly scalable thermal or insulation solution for medium-voltage operation. Instead, its purpose is to validate the core transformer concept, including the winding structure, transformer topology, and winding arrangement under representative electrical and magnetic operating conditions. The applicability of the results therefore lies primarily at the architectural and electromagnetic design level, while full-scale insulation coordination and thermal design must be addressed separately in practical implementations.

From a state-of-the-art perspective, this work advances existing studies by shifting the focus from isolated analytical optimization to experimentally validated, application-driven transformer design, with emphasis on winding realization, insulation assessment, and test methodology for medium-voltage SST systems.

The rest of this article is organized as follows. Section II introduces the selected SST topology and discusses the system-level context of the transformer. Section III reviews

the applied standards and outlines the transformer design procedure. Section IV presents the optimization workflow and the selection of the final design. Section V describes the electromagnetic simulations. Sections VI and VII detail the prototype fabrication and experimental results, respectively. Finally, Section VIII concludes this article.

II. TOPOLOGY SELECTION

The design of the MFT in an SST is closely linked to the choice of topology. Cascaded and DAB configurations are typically more appropriate for small- to medium-scale applications, such as grid-connected solar panels or microgrids in residential and community settings [32], [33], [34]. For large-scale SST systems, MMC topologies are generally more suitable due to their scalability and ability to handle higher power and voltage levels [3].

An extensive comparison between different topologies such as ISOP, MMC, and resonant MMC (MMR) is given in [3]. For the present study, the MMR topology has been selected due to its lower overall system weight, compact transformer design at higher operating frequency, reduced harmonic distortion in resonant currents, and balanced tradeoff between size, efficiency, and complexity.

The overall system architecture is illustrated in Fig. 1. A medium-voltage input is connected to a phase-shifting autotransformer, which provides the required phase displacement for harmonic reduction. The output of the autotransformer is supplied to a 12-pulse diode rectifier unit (DRU). An interphase transformer is included to combine the rectified outputs and improve current sharing between the rectifier bridges. The rectified DC voltage u_{dc} and current i_{dc} are then applied to the MMR converter.

The MMR converter is composed of modular submodules (SMs) arranged in converter arms with arm inductors L_{arm}. Resonant components, including the resonant capacitor C_r and the leakage and magnetizing inductances of the MFT, form the resonant tank that enables soft-switching operation. The MFT provides galvanic isolation and voltage scaling between the converter and the load side.

On the secondary side of the MFT, DRU are used to generate the DC output required by the electrolyzers. In this configuration, a six-pulse DRU is employed, which delivers the appropriate DC voltage and current for hydrogen production. The modular arrangement allows operation at medium frequency, reduces transformer size, and facilitates efficient power transfer from the medium-voltage grid to the electrolyzers.

III. TRANSFORMER DESIGN

The design and analysis of medium-voltage, MFTs require adherence to international standards to ensure safety, reliability, and performance. In this section, the standards used for the design, testing, and validation of the transformer are introduced. These standards provide guidelines for parameters, such as insulation coordination, temperature rise limits, PD measurement, and test procedures. Following these standards ensures that the transformer design aligns with industrial requirements and facilitates comparison with other designs reported in the literature.

TABLE 3. Summary of Applied Standards

Standard	Scope	Application in This Work
IEC 60076 [27]	Design, testing, and operation of power transformers	Verification of electrical, thermal, and insulation performance of MV-MFT
IEC 60270 [28]	Measurement of PD under AC/DC voltages	Evaluation of insulation performance and PD acceptance verification
IEEE 519 [29]	Voltage and current harmonic distortion limits at PCC	Definition of harmonic control objectives for SST and converter interfaces

A. STANDARDS

The main international standards applied in this study are reviewed in Table 3. These include the IEC 60076 [27] series for transformer design and testing, IEC 60270 [28] for PD measurement, and IEEE 519 [29] for harmonic control at the point of common coupling (PCC).

The IEC 60076 series specifies requirements for the design, testing, and operation of power transformers. It provides guidelines for transformer construction, insulation coordination, temperature rise limits, dielectric testing, and operational constraints. In this work, IEC 60076 is applied to verify that the medium-voltage, MFT complies with established industry practices. The series covers both oil-immersed and dry-type transformers and supports validation of the electrical, thermal, and insulation performance of the proposed designs.

PD measurement is an essential diagnostic and quality assessment method for high-voltage equipment, providing insight into insulation integrity and aging behavior. IEC 60270 specifies the procedures for measuring PD under AC and DC voltages, including test circuits, calibration methods, and measurement practices. In this study, IEC 60270 is applied during design validation to evaluate insulation performance and ensure that the proposed transformer design satisfies internationally recognized acceptance criteria.

IEEE 519-2022 defines limits for voltage and current harmonic distortion at the PCC. Compliance with this standard ensures compatibility of power electronic systems with the grid and protection of sensitive loads. In this study, IEEE 519 is used to establish harmonic control objectives for the SST and its power electronic interfaces. This choice is motivated by the standard's widespread adoption in power electronic system design, and its detailed practical guidelines for harmonic management in converter-based applications.

B. DESIGN

The insulation distances and cooling assumptions used in the prototype are selected to ensure safe laboratory operation and compliance with relevant standards at reduced voltage and power levels, rather than to replicate the final medium-voltage insulation and thermal design. The design procedure is

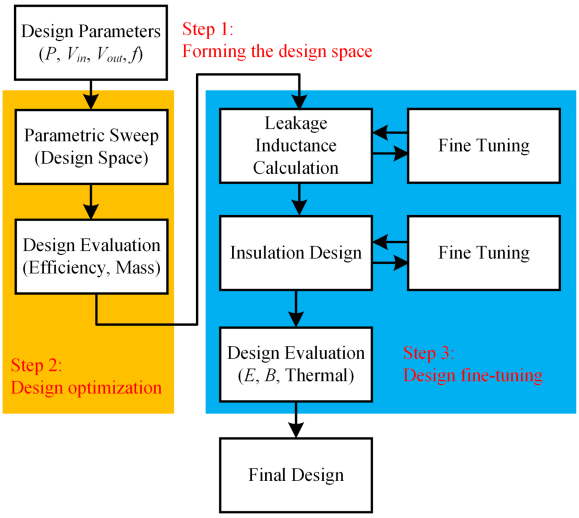

FIGURE 2. Design pipeline.

performed in three main steps, as shown in Fig. 2. The design procedure is as follows.

1) *Design space reduction:* An analysis is performed on the analytical behavior of an MFT, and based on the constraints imposed by the design requirements, saturation behavior, and international standards, a finite design space is identified. This includes the most important parameters that affect the mass–efficiency profile of the MFT and allows to reduce the computational complexity of the iterative optimization in the following step. The result is a table containing all the necessary parameters for modeling the MFT and evaluating it in terms of mass and efficiency via analytical and FEM simulations.
2) *Topology optimization:* For each design entry previously defined, an FEM geometrical model is generated. Simulations are performed to compute load and core losses at 1 kHz, as well as total transformer mass. The result is a plot displaying the mass–efficiency distribution of each design within the effective design space. As the optimum design also must satisfy the required series inductance for the selected topology, the value of the leakage inductance is taken into account for design selection.
3) *Design fine tuning and verification:* Based on the previous plot distribution, a candidate design is selected and undergoes FEM simulation to verify and fine tune internal behavior. This includes core saturation, electric field intensity in the insulation, and thermal rise behavior.

1) WINDING DEIGN

In order to perform the winding analysis, a base case is selected and then further developed for additional options, using a secondary number of turns equal to four. For the base case, the number of primary turns is calculated as 185, based on the required transformer ratio of 46.2.

The phase currents on the primary and secondary sides are derived as

$$I_p = \frac{I_{pL}}{\sqrt{3}} = \frac{7.07}{\sqrt{3}} = 4.08\,\text{A} \tag{1}$$

$$I_s = \frac{I_{sL}}{\sqrt{3}} = \frac{326.6}{\sqrt{3}} = 188.56\,\text{A}. \tag{2}$$

To account for overcurrent scenarios, a safety margin of 10% is used; therefore, the design current values are 4.5 A (primary) and 207 A (secondary). The conductor cross-sectional area is constrained by a maximum current density of 4 A/mm^2. It follows that the minimum surface area required for the primary conductor is

$$a_p = \frac{I_p}{J_{p,\max}} = \frac{4.08}{4} = 1.02\,\text{mm}^2. \tag{3}$$

At elevated frequencies, the skin effect becomes significant, limiting current penetration into the conductor. For a copper conductor operating at 1 kHz, the skin depth is given by

$$\delta = \sqrt{\frac{\rho}{\pi \mu f}} \approx \frac{0.066}{\sqrt{f}} = 2.087\,\text{mm} \tag{4}$$

where μ and σ represent the permeability and electrical conductivity of the material, respectively. Maintaining conductor dimensions within 4 mm ensures that the skin effect remains negligible. To ease the winding and assembly procedure, a rectangular conductor is selected.

Due to the large number of turns, the primary winding is constructed using two disk types: Type 1 (multiturn) and Type 2 (single-turn). In particular, the single-turn Type 2 disks are placed at locations where the conductor is brought into or out of the disk stack, providing a dedicated, well-defined path for the lead. This prevents overlap between the transition lead and the adjacent turns of the neighboring disk and helps maintain the intended interdisk clearance. This modular winding approach simplifies the construction process and conductor placement on the bobbin. Each Type 1 disk contains 14 turns. A total of 16 Type 1 and 15 Type 2 disks yield 239 turns. To reach the required 185 turns, eight Type 1 disks are reduced by one turn each.

Spacing assumptions include 1 mm between turns and 2 mm between disks. An additional 2 mm margin is added on either side to accommodate the bobbin structure. The interdisk gap (G_{dd}) is set at 4.2 mm.

For the secondary winding, an important consideration is to distribute the high current across multiple parallel paths to reduce conduction losses. An initial estimate assumes 15 parallel conductors, resulting in approximately 14 A per path. To maintain the current density within the maximum allowable limit of 4 A/mm^2, the minimum conductor cross-sectional area is calculated as

$$a_s = \frac{I_{\text{per path}}}{J_{\max}} = \frac{14}{4} = 3.5\,\text{mm}^2. \tag{5}$$

Spacing between turns and between adjacent parallel paths is chosen such that the overall cross-sectional dimensions of the

primary and secondary windings remain comparable, ensuring symmetry in magnetic coupling and thermal behavior.

2) CORE DESIGN

At the operating frequency of 1 kHz, conventional core materials, such as ferrite and electrical steel, are generally unsuitable due to significant eddy current losses. However, for the prototype developed in this study, electrical steel has been selected considering its availability, mechanical robustness, and ease of fabrication.

GOES has maximum flux density up to 2.0 T; however, due to high-frequency losses, $B_m = 1.8$ T is considered for the design of the core's cross-section area to maintain a safety margin and avoid core saturation. Using this value, the minimum required core cross-sectional area is calculated as

$$A_c = \frac{\int V\,dt}{k_c B_m N_p} = \frac{0.6}{0.79 \times 1.8 \times 185} = 2916\,\text{mm}^2 \quad (6)$$

where $k_c = 0.54$ is the stacking factor for the selected lamination thickness. Assuming a square cross section, this corresponds to a minimum core leg width of approximately 54 mm.

Core window dimensions are topology-dependent and will be refined in later stages of the design. The maximum operating voltage of the transformer is 2.45 kV, corresponding to the 3.6 kV insulation class according to IEC 60076-11. Based on this classification, the dielectric design is governed by the 50/60 Hz applied voltage withstand requirement of 10 kV (rms, 1 min), while lightning impulse (LI) testing is not applicable, as the transformer is intended for controlled laboratory operation and is not exposed to atmospheric or network-related overvoltages. At this stage of the design, conservative insulation and spacing assumptions are adopted from the minimum insulating distances specified in IEC 60076-11, namely a core leg-to-phase gap $G_{pl} = 20$ mm, interphase gap $G_{pp} = 20$ mm, core yoke-to-phase gap $G_{py} = 20$ mm, and primary-to-secondary gap $G_{ps} = 20$ mm. These values provide sufficient margin for the applied voltage test and allow flexibility for later refinement of the core window dimensions, which are topology-dependent. It is noted that the minimum distance between the core leg and the winding occurs along the diagonal of the square core cross section, which is explicitly considered in the insulation coordination.

Based on the selected winding dimensions, 130 mm in height and 17 mm in width for both primary and secondary windings, the core window sizes can be estimated for each configuration listed previously. This provides a preliminary framework for evaluating the available design options.

IV. OPTIMIZATION

The optimization block diagram is shown in Fig. 3. The optimization procedure is as follows.

The design tables are generated in MATLAB. Based on the design space identified in the previous section, a design table is created by the permutations of parameters (conductor material and size, number of secondary turns, window and

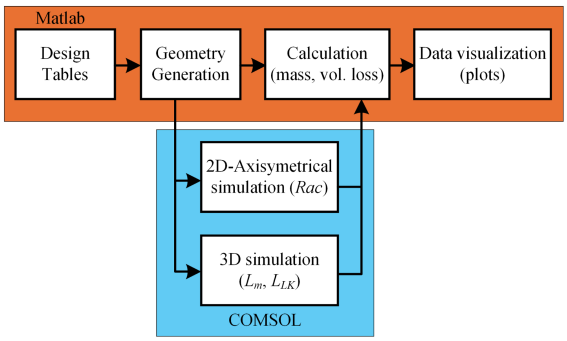

FIGURE 3. Optimization block diagram.

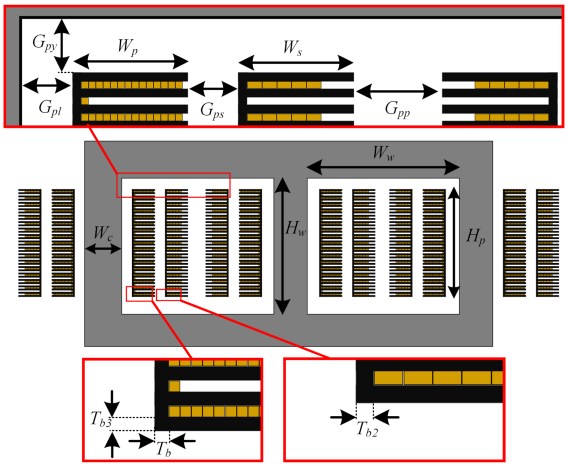

FIGURE 4. Dimensions of the transformer.

core size, etc). The result is a table containing approximately 1800 designs.

A design sweep algorithm is implemented in MATLAB to systematically evaluate a set of candidate designs. For each entry in the design table, the algorithm generates the necessary parameters for geometric modeling and creates a corresponding COMSOL simulation to evaluate the winding AC resistance. The efficiency and total mass of each design are computed. The results are presented in a mass-efficiency plot to identify optimal tradeoffs for to the requirements. The process begins with calculating the core's geometric dimensions to determine its mass and to enable accurate model generation in COMSOL.

The dimensions of the transformer are shown in Fig. 4. From the data provided in the design table, the code computes the dimensions of the core window as

$$W_w = 2 \times \left(G_{pl} + T_b + W_p + T_{b2} + G_{ps} + T_b + W_s + T_{b2} + \frac{G_{ww}}{2} \right) \quad (7)$$

$$H_w = 2 \times \left(G_{wy} + T_{b3} \right) + H_p. \quad (8)$$

From the calculated window size and core width, the total core volume can be determined (a scaling factor of 0.99 is

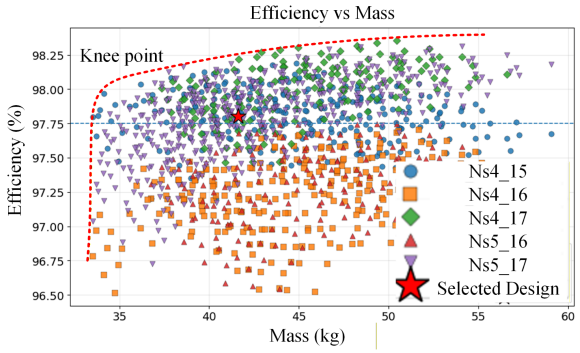

FIGURE 5. Optimization results for efficiency versus mass. The selection is made by mass–efficiency optimum point satisfying minimum required leakage inductance.

applied to compensate for rounded edges)

$$V_c = 0.99\,[(2W_w + 3W_c)(H_w + 2W_c) - 2(H_w W_w)]\,W_c. \quad (9)$$

The core mass is then calculated using the electrical steel density $\rho_c = 7.3\,\mathrm{g/cm^3}$

$$M_c = V_c \times \rho_c. \quad (10)$$

The conductor length is approximated as the product of the number of turns and the average turn length in each winding, allowing the mass of each conductor to be estimated as

$$M_p = 3 \times l_p \times W_{cp} \times H_{cp} \times \rho \quad (11)$$

$$M_s = 3 \times P_{PS} \times l_s \times W_{cs} \times H_{cs} \times \rho \quad (12)$$

where W_{cp} and W_{cs} are the width of conductors of primary and secondary, respectively, and H_{cp} and H_{cs} define the height of conductors in primary and secondary, respectively. Therefore, the total mass of the transformer, excluding insulation and terminations, is

$$M_t = M_c + M_p + M_s. \quad (13)$$

Using COMSOL LiveLink for MATLAB, an FEM simulation is performed to compute the AC losses at 1 kHz for both conductors. Once the conductor AC resistance is obtained, the load losses for the primary and secondary windings at 1 kHz are calculated as

$$P_p = 3 \times R_p \times I_p^2 \quad (14)$$

$$P_s = 3 \times R_s \times I_s^2. \quad (15)$$

Core losses are estimated analytically using the following equation [35]:

$$P_c = W_c \times P_{c0} \left(\frac{f}{f_0}\right)^{\alpha} \left(\frac{B_m}{B_{m0}}\right)^{\beta} \left(\frac{k_f}{k_{f0}}\right)^{2(\alpha-1)}. \quad (16)$$

The transformer total efficiency is computed as

$$\eta = \frac{25\,\mathrm{kW}}{25\,\mathrm{kW} + P_c + P_p + P_s}. \quad (17)$$

The results for each design configuration are summarized in Fig. 5. It should be noted that although the turns ratio is fixed by the required voltage transformation (approximately 46.2), the absolute number of turns is not unique and can be scaled while maintaining the same ratio, provided that the minimum number of turns required to avoid core saturation is respected. For example, equivalent ratios can be achieved using configurations, such as $N_p = 185$, $N_s = 4$ or $N_p = 213$, $N_s = 5$. This design flexibility was intentionally explored because leakage inductance strongly depends on the number of turns; increasing the number of turns increases it. Since the leakage inductance serves as the required series inductance in the *LLC* resonant tank, the number of turns was treated as an optimization variable. From the plot, it can be observed that designs with five secondary turns and either 15 or 17 parallel paths in the secondary winding yield the highest efficiency. This confirms the trend observed during the initial analysis, where configurations with five secondary turns exhibited a notable reduction in mass compared to those with four turns. The knee point in the efficiency–mass curve represents the optimal tradeoff between performance and weight. It corresponds to a region of diminishing returns in the efficiency–mass distribution, where further increases in mass result in only marginal improvements in efficiency. This region is highlighted in Fig. 5.

It should be noted that operation at 1 kHz represents an intermediate-frequency regime, where losses associated with high-frequency effects become significant while the size reduction benefits of very high-frequency operation are not fully realized, leading to a natural efficiency tradeoff.

It is essential to ensure that the leakage inductance remains within the required range of approximately 9 mH. To verify this, a subset of designs with total mass between 35 and 42 kg and efficiency above 98% is selected, and a 3-D COMSOL simulation is performed for each configuration. Among the evaluated candidates, the lightest design that satisfies the leakage inductance requirement is identified as ID-365 (where ID denotes the internal design identifier assigned to each candidate configuration). In addition, a heavier alternative, ID-122, exhibits comparable leakage inductance values of 7.7 mH for the side phases and 10.2 mH for the central phase.

The small dispersion in leakage inductance between the outer and central phases is inherent to three-limb core geometries. The central leg shares its return flux with both side legs and therefore experiences a slightly different magnetic environment and fringing field pattern compared to the outer legs. In addition, the discrete modular winding arrangement and the finite window width cause minor differences in the spatial distribution of leakage flux from phase to phase. These effects result in a few-percent variation of the computed leakage inductances, which is typical for three-phase core-type transformers and is acceptable for the targeted SST application.

The key distinction between the two designs lies in the conductor material: ID-365 employs aluminum, achieving an efficiency of 97.5% at a total mass of 38.4 kg, while ID-122 uses copper, reaching 97.8% efficiency at 41.6 kg. Although the aluminum-based design offers a clear advantage in terms

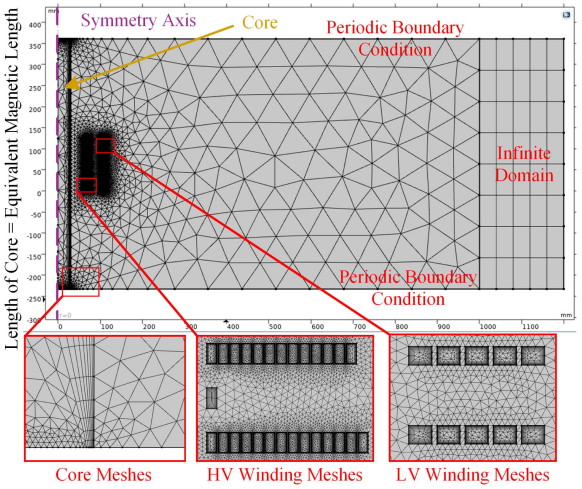

FIGURE 6. COMSOL geometry and mesh for magnetic fields simulation.

of reduced mass, its integration presents several practical challenges due to material incompatibility with the copper-based PECs and the resonant converter interface. With these considerations in mind, Design 122 is selected as the final configuration.

V. SIMULATION

With the candidate design selected, detailed simulations are performed to analyze the internal electric and magnetic field distributions. To evaluate the magnetic field distribution within the core, a 2-D axisymmetric FEM model is implemented using COMSOL Multiphysics. The simulation is performed at an operating frequency of 1 kHz and focuses on a single transformer phase, including the polycarbonate (PC) bobbins, to reduce computational complexity. The simulation geometry and meshing strategy are illustrated in Fig. 6. The worst-case conditions are expected to occur at the region of minimum distance between the core leg and the surrounding structure, particularly at the 45° angular position. Due to the axisymmetric nature of the simulation, the rectangular core is approximated as a cylindrical shape.

The equivalent radius of the cylindrical core model is calculated using the core flux utilization factor k_f as

$$R_{eq} = W_c \times \sqrt{2} \times k_f. \tag{18}$$

To preserve the magnetic path length, the height of the core leg is adjusted according to

$$H_c = 1.5 \times (H_w + W_c) + W_w + W_c \tag{19}$$

where H_w and W_w are the window height and width, respectively, and W_c is the core width.

A periodic boundary condition is applied to the surrounding air domain to simulate an infinite repeating structure. The material properties used in the simulation are summarized in Table 4. Notably, the core is modeled as a solid block with an equivalent electrical conductivity to account for lamination

TABLE 4. Material Properties Used in Magnetic Field Simulation

Material	μ_r	σ [S/m]	ε_r
Air	1	1×10^{-5}	1
Copper	1	4.2×10^{7}	∞
Core	4×10^{3}	2963	∞
PC	1	1×10^{-13}	2.6

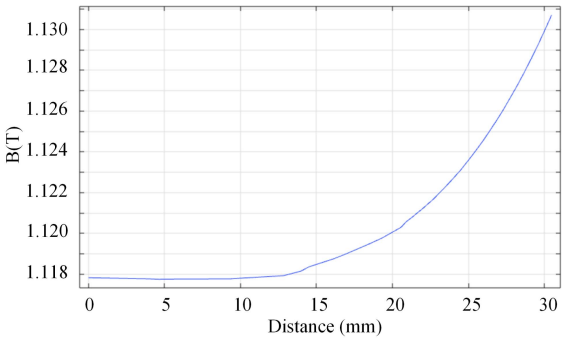

FIGURE 7. Magnetic field intensity within the core leg, measured along the cut-line in the core.

effects [36]. The adjusted conductivity is calculated as

$$\sigma_c = \frac{44 \times 10^6}{(R_{eq}/w_l)^2} \tag{20}$$

where $R_{eq} = 30.46$ mm and $w_l = 250\,\mu$m, yielding an effective conductivity of $\sigma_c = 2963$ S/m.

The resulting magnetic field distribution is shown in Fig. 7. The peak magnetic flux density within the core reaches 1.13 T, remaining below the material's saturation threshold and providing a safety margin for overvoltage and transient conditions.

The electric field distribution within the transformer air gaps is also investigated. For this simulation, a single window and phase are modeled using a 2-D electrostatics study, as illustrated in Fig. 8. The study evaluates steady-state field conditions under worst-case voltage stress, corresponding to the peak primary-side excitation.

Across most of the domain, the electric field magnitude remains below 0.4 kV/mm. A localized peak of approximately 1.8 kV/mm is observed near sharp conductor edges. Although this value exceeds the dielectric strength threshold, the simulation does not account for the presence of enamel insulation on the wires.

VI. PROTOTYPING

The first step in the fabrication process is the 3D-printing of the PC bobbins for support of the conductors. In order to meet supplier availability, the secondary conductor size was changed to 2.8 mm × 1.8 mm. Since the surface area remains unchanged, the only modification required was a slight enlargement of the bobbin guides.

Once the bobbins are printed, the conductor is wound around the guides. In order to maintain tension on the wire and

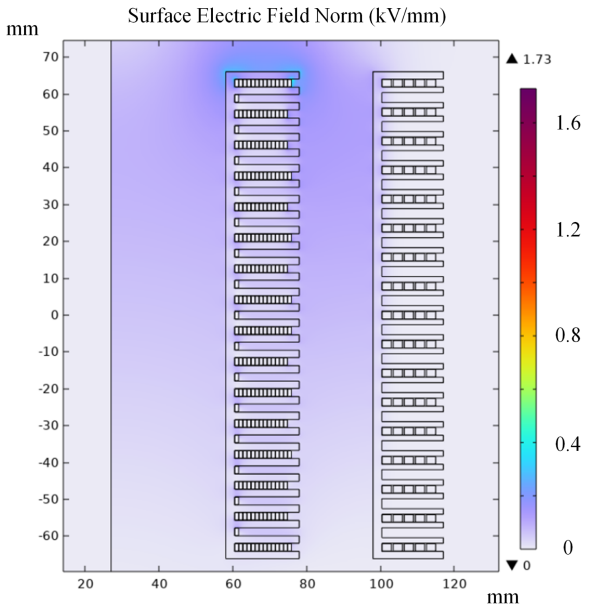

FIGURE 8. Electric field magnitude around primary coil.

TABLE 5. Core Material Properties

Material	Lamination Thickness [mm]	Max Core Losses at 1.5 T [W/kg]	Min Magnetic Polarization
M400-50A	0.50	4.0	1.53 T at 2500 A/m
H085-23	0.23	0.6	1.90 T at 900 A/m

ensure minimal spacing between turns, where high electric fields could arise, the bobbin is placed above the copper wire reel. While rotating the PC bobbin and winding the conductor, tension is maintained using the weight of the copper itself.

Terminations are then added to the secondary coils, connecting each parallel path using a 25 mm × 3 mm copper bus bar. Special attention is required to avoid external particles from the workshop environment polluting the assembly, as these imperfections can cause local increases in electric field and degrade performance, possibly resulting in local discharges or breakdown.

Two material options are chosen for magnetic core fabrication: H085-23 (GOES) [37] and M400-50 A [nongrain-oriented electrical steel (Non-GOES)] [38]. Table 5 lists the material properties provided by the manufacturer, showing how the grain-oriented material results in lower losses due to the molecular arrangement. This makes GOES ideal for magnetic cores in transformers, where the magnetic flux is predictable and aligned with the crystalline structure. On the other hand, nongrain-oriented steel possesses random orientation of the material crystals, resulting in higher losses, especially at higher frequencies, but with reduced material cost.

While the performance of GOES and Non-GOES at higher frequencies is reduced compared to amorphous materials,

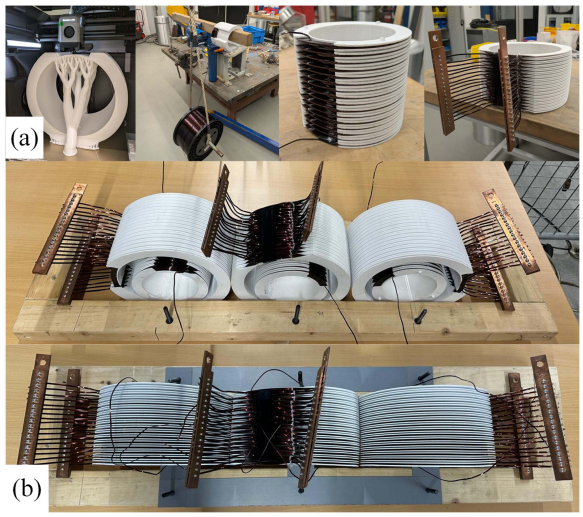

FIGURE 9. Fabrication and assembly stages of the modular transformer windings: (a) fabrication of the 3D-printed support structure and winding setup and (b) preparation and stacking of individual modular winding segments, electrical interconnection and alignment of the winding modules using busbar terminals, and final assembly of the three-phase winding structure prior to core integration.

FIGURE 10. Assembled MFT with winding modules secured and core clamped in place.

such as Metglas, electrical steel cores are a more economical alternative that can be effectively used for insulation testing [31]. The steel core assembly can then be used for three-phase PD testing, applied voltage testing, and other loading tests, as suggested in the next section. A study can then be performed comparing the effectiveness and suitability of GOES and Non-GOES magnetic cores for medium-frequency applications.

Through-hole screws are used to assemble the structure and maintain pressure across the sheets, minimizing the inter-lamination gap/interface. The dimensions of each strip are as follows: during the assembly process, the phase coils are inserted onto the construction, and insulation distances are maintained using PC spacers.

The transformer fabrication process is shown in Fig. 9. The assembly begins by preparing a wooden frame to hold the components in place during construction. The preformed modular winding segments are then positioned on the frame in their designated locations. The winding terminals are aligned and connected according to the required electrical configuration. Once the windings are secured, the laminated magnetic

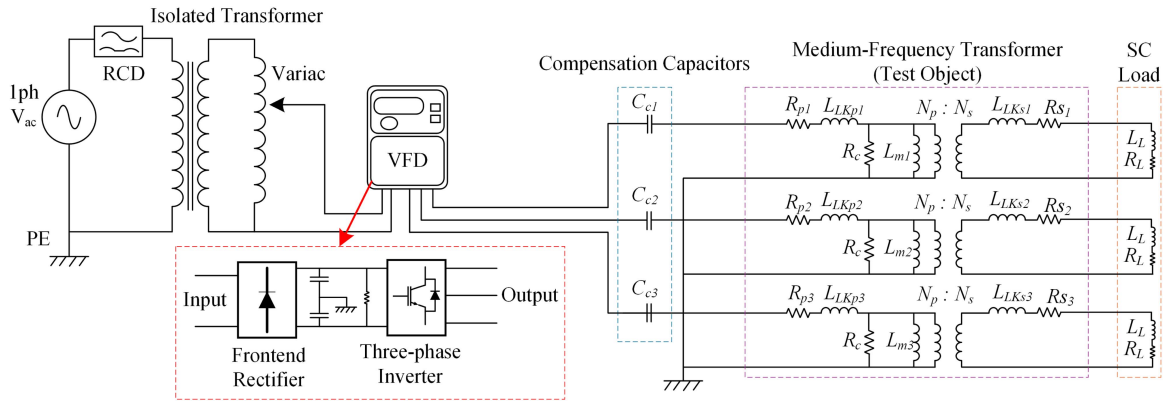

FIGURE 11. Experimental setup for three-phase excitation of the MFT using a single-phase-fed VFD. Each phase is series-compensated with a tuned capacitor to achieve resonance at the operating frequency. Three high-value resistors (R_{vg}) form a virtual-neutral network connected at the transformer side of the capacitors to stabilize the floating star point without tripping the RCD protection.

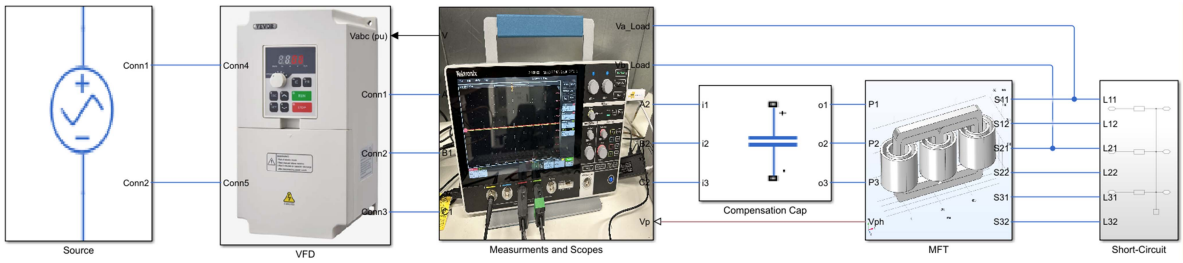

FIGURE 12. System-level Simulink circuit used to generate the results shown in Fig. 14. The circuit corresponds to the experimental setup illustrated in Fig. 11, including the series compensation capacitors and three-phase MFT model.

core segments are inserted through the coil openings to complete the magnetic path. The structure is finally tightened to ensure proper mechanical stability and electrical insulation before further testing. The assembled MFT is shown in Fig. 10.

VII. EXPERIMENTAL RESULTS

A. SHORT-CIRCUIT TEST

The verification of the electrical design targets is performed by comparing analytical and simulation-based predictions with experimental measurements. The leakage inductance requirement, defined during the design stage to satisfy the resonant operation of the selected SST topology, is validated through frequency-response measurements under short-circuit conditions. The measured impedance minimum around the target operating frequency of 1 kHz is used to confirm that the designed leakage inductance is achieved. Loss-related behavior is evaluated by comparing measured current waveforms and impedance characteristics with analytical and FEM-based estimates obtained during the optimization stage.

As shown in Fig. 11, the setup of the short-circuit test consists of six parts as follows:

1) *50 Hz grid* and protection;
2) *50 Hz insulation transformer and Variac* to isolate the circuit and ramp up the applied voltage to the test circuit;

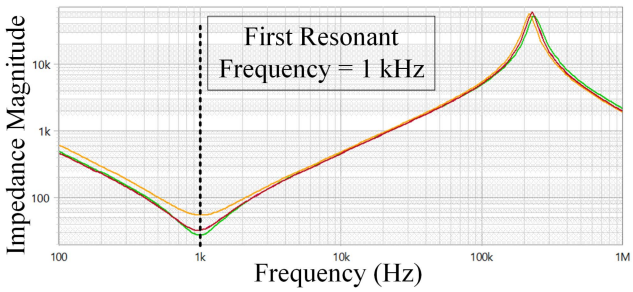

FIGURE 13. Measured frequency response of the transformer under short-circuit conditions using the Bode 100 VNA.

3) *measurement equipment*, including oscilloscope, current probes, differential voltage probes;
4) *compensation capacitors* to set the resonant frequency at 1 kHz for short-circuit test;
5) *MFT* assembled as shown in Fig. 10;
6) *short-circuit connection* to provide low-impedance load for the MFT to mimic the real short-circuit situation.

The system-level circuit used for the simulation corresponds directly to the experimental setup shown in Fig. 11 and is illustrated in Fig. 12. The frequency response of the transformer, measured by Bode 100 vector network analyzer (VNA), in case of short-circuit is shown in Fig. 13. The impedance response shows a characteristic minimum around

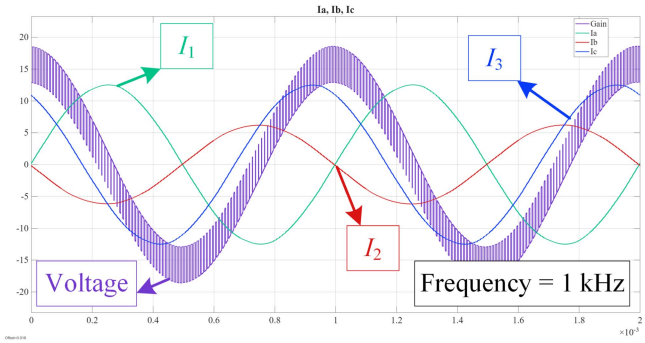

FIGURE 14. Simulated phase currents I_a, I_b, and I_c and primary-side voltage waveform at 1 kHz obtained from the system-level Simulink model with series-compensation capacitors.

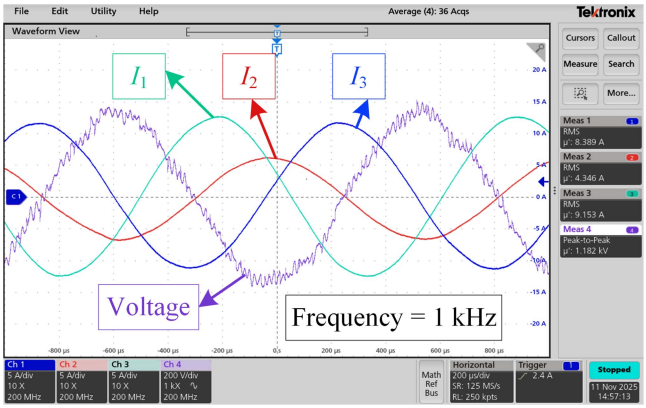

FIGURE 15. Experimental waveforms of the three-phase currents I_1–I_3 and primary voltage of the prototype MFT during the 1 kHz short-circuit test.

1 kHz, corresponding to the short-circuit condition used for validation. At higher frequencies, the impedance increases due to leakage inductance, reaching a resonance peak near 120 kHz, which results from the interaction between the transformer leakage inductance and stray capacitances. To verify the analysis, especially for the compensation capacitors, a system-level Simulink simulation has been implemented as shown in Fig. 14. The experimental results are shown in Fig. 15. The test setup is shown in Fig. 16.

As can be seen from Fig. 15, the three phase currents are not perfectly identical. The small deviation in amplitude is consistent with the leakage inductance differences between the outer and central phases obtained from the FEM analysis. In three-limb core-type transformers, the central leg naturally has a slightly different leakage path and mutual coupling than the outer legs, leading to a small dispersion in phase reactances.

B. THERMAL EVALUATION

In addition to the electrical and insulation validation, an experimental thermal assessment of the fabricated prototype was performed to evaluate the temperature distribution under representative operating conditions. Infrared thermography

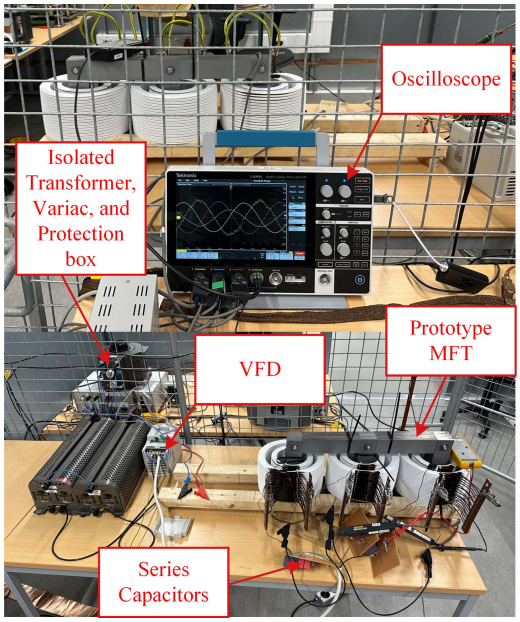

FIGURE 16. Laboratory setup for three-phase short-circuit testing of the prototype MFT at 1 kHz: (top) front view with oscilloscope displaying the measured phase currents and voltage waveforms, and (bottom) overview of the complete test bench including supply, compensation capacitors, load resistors, and measurement equipment.

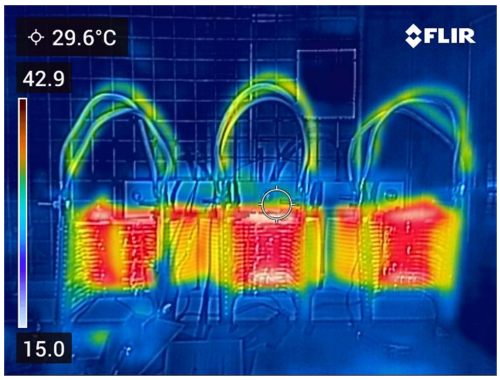

FIGURE 17. Infrared thermography image of the fabricated three-phase MFT during operation.

measurements were carried out using a FLIR thermal camera during steady-state operation.

Fig. 17 shows the measured thermal profile of the three-phase transformer. The results indicate that the temperature rise remains moderate, with the highest temperature observed at approximately 42 °C–43 °C at the winding region. The thermal distribution is relatively uniform across phases, and no localized hotspots or abnormal heating were observed.

It is noteworthy that the imbalance between the phases can be compensated during normal SST operation by the control scheme of the MMC converter, which actively regulates the phase currents and mitigates small impedance differences. However, in the experimental setup of Fig. 11, a variable frequency drive (VFD) is used as the excitation source; therefore, active balancing through converter control is not available. To

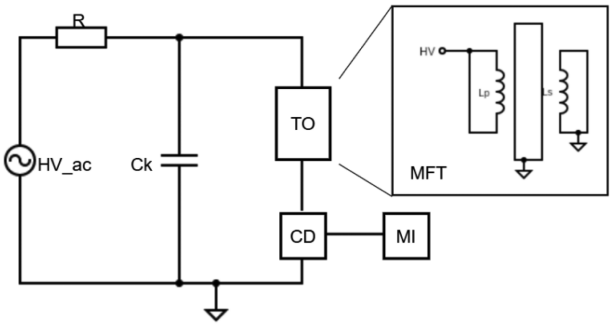

FIGURE 18. PD test setup diagram, showing the TO, CD, and MI. The h primary coil is connected to the HV source at both connections, ensuring no turn-to-turn voltage; secondary winding and core are connected to ground.

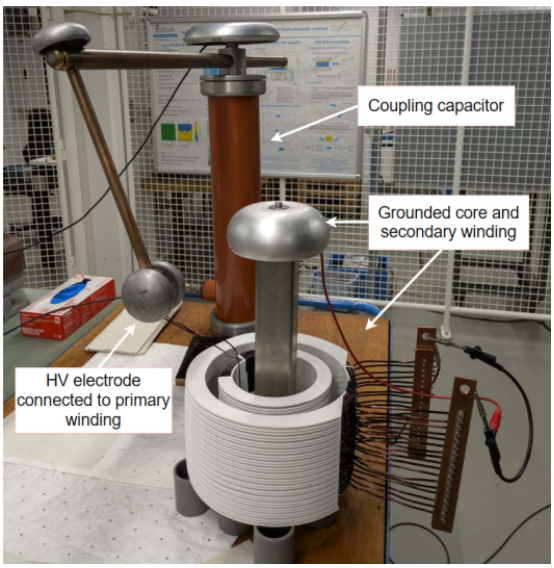

FIGURE 19. PD physical setup.

compensate for the inherent impedance differences between the outer and central phases at the resonant frequency, two additional series inductors are introduced in the side phases. This adjustment enables improved current balancing during operation and ensures that the thermal test conditions shown in Fig. 17 represent, as closely as possible, the expected operating conditions of the SST under balanced loading.

C. PD MEASUREMENT

The PD measurement is conducted under 50 Hz condition using conventional test setup depicted in Fig. 18. The PD pulses generated in the transformer's insulation system are extracted via a coupling device (CD), typically a high-frequency measuring impedance, and fed into a measuring instrument (MI) for analysis. The secondary winding and core are grounded to prevent undesired induction.

A photograph of the physical test setup is provided in Fig. 19. The applied voltage waveform and the corresponding PD measurement are shown in Fig. 20. During the test, the applied voltage is first increased to $1.8 \times U_r$, where U_r denotes

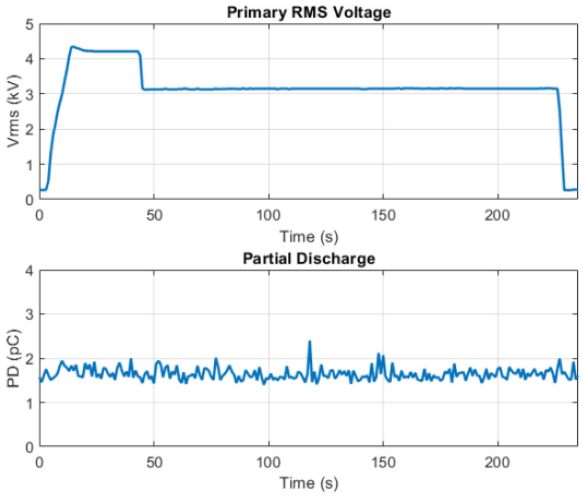

FIGURE 20. Time evolution of the primary rms voltage (top) and measured PD magnitude (bottom) based on the method detailed in IEC 60270 [28] and IEC 60076 [39].

the rated rms voltage of the test object (TO), and maintained for 30 s. The voltage is then reduced to $1.3 \times U_r$ and held for 180 s before being decreased to zero. Throughout the test, the PD level is continuously monitored. As the measured PD level remains well below 10 pC, the test is considered passed, confirming that the air and wire enamel insulation are sufficient to withstand the applied voltage, even under temporary over voltage conditions.

VIII. CONCLUSION

This work presented the design, optimization, prototyping, and experimental validation of a downscaled medium-voltage, MFT intended for SST applications in large-scale hydrogen production systems. The prototype was developed to verify the electrical, magnetic, and thermal performance of a full-scale design at reduced power levels.

A systematic design methodology was followed, combining analytical calculations, FEM simulations, and optimization using MATLAB–COMSOL integration. The selected configuration achieved a balance between efficiency, weight, and leakage inductance. The fabricated prototype was tested under short-circuit and PD conditions. The impedance measurements confirmed the expected resonance behavior, and the PD test results verified sufficient insulation performance under high-voltage stress.

Overall, the experimental results confirm that the proposed MFT design meets the functional and insulation requirements, demonstrating scalability toward full-scale implementation in medium-voltage SST systems for hydrogen production applications.

REFERENCES

[1] Z. Li et al., "Comparison of modular multilevel converter based solid state transformer for AC/DC application," in *Proc. IECON 2023- 49th Annu. Conf. IEEE Ind. Electron. Soc.*, 2023, pp. 1–6, doi: 10.1109/IECON51785.2023.10312314.

[2] R. Mirzadarani et al., "Three-phase medium-voltage medium-frequency transformer for SST in green hydrogen production," in *Proc. IECON 2023- 49th Annu. Conf. IEEE Ind. Electron. Soc.*, 2023, pp. 1–6, doi: 10.1109/IECON51785.2023.10312546.

[3] Z. Li et al., "Medium-voltage solid-state transformer design for large-scale H2 electrolyzers," *IEEE Open J. Power Electron.*, vol. 5, pp. 936–955, 2024, doi: 10.1109/OJPEL.2024.3414151.

[4] Z. Li et al., "Novel control strategy for modular multilevel resonant converter based solid-state transformer," in *Proc. PCIM Conf. 2025; Int. Exhib. Conf. Power Electronics, Intell. Motion, Renewable Energy Energy Manage.*, 2025, pp. 794–799, doi: 10.30420/566541100.

[5] Z. Deng et al., "Efficiency improvement of solid-state transformers with MMC front-end AC–DC converters through adjusting DC bus voltage and active cells," *IEEE Trans. Power Electron.*, vol. 39, no. 10, pp. 13218–13233, Oct. 2024, doi: 10.1109/TPEL.2024.3424891.

[6] S. Farzamkia, M. Zhang, H. Zou, A. Vetrivelan, and A. Q. Huang, "MMC based solid state transformer for large-scale distributed PV integration and medium voltage AC/DC interconnection," *IEEE Trans. Power Del.*, vol. 39, no. 4, pp. 2495–2506, Aug. 2024, doi: 10.1109/TPWRD.2024.3417807.

[7] M. Rashed Hassan Bipu et al., "Design, control, and protection of a 13.2 kV, 1 MVA solid state transformer for electric vehicle extreme fast charging station," *IEEE Trans. Transport. Electrific.*, vol. 11, no. 1, pp. 4469–4481, Feb. 2025, doi: 10.1109/TTE.2024.3462920.

[8] S. Rajendran and A. Q. Huang, "Design, analysis, and implementation of a 500-kVA hybrid solid-state transformer," *IEEE Trans. Emerg. Sel. Topics Power Electron.*, vol. 13, no. 5, pp. 5734–5748, Oct. 2025, doi: 10.1109/JESTPE.2025.3593320.

[9] A. Cervone, Z. Li, and D. Dujic, "Modularized diode rectifiers: A new family of solid-state transformers," *IEEE Trans. Power Electron.*, vol. 40, no. 4, pp. 4747–4751, Apr. 2025, doi: 10.1109/TPEL.2024.3520237.

[10] A. Meligy, R. Coelho-Medeiros, I. Colak, and S. Bacha, "Mission profile-based reliability assessment for modular MVAC-LVDC solid-state transformers," *IEEE Access*, vol. 13, pp. 151736–151757, 2025, doi: 10.1109/ACCESS.2025.3603095.

[11] A. Khan, S. S. Nag, and B. Singh, "A three-phase unfolding-based solid-state traction transformer for railway application," *IEEE Trans. Power Electron.*, vol. 40, no. 5, pp. 7439–7452, May 2025, doi: 10.1109/TPEL.2025.3529467.

[12] S. Zhao, Q. Li, F. C. Lee, and B. Li, "High-frequency transformer design for modular power conversion from medium-voltage ac to 400 vdc," in *IEEE Trans. Power Electron.*, vol. 33, no. 9, pp. 7545–7557, Sep. 2018, doi: 10.1109/TPEL.2017.2774440.

[13] T. Hatakeyama, N. Kurita, and M. Kimura, "Prototyping of 500 kVA medium frequency transformer for offshore direct-current collection grid," in *Proc. Int. Power Electron. Conf. (IPEC-Niigata 2018 -ECCE Asia)*, 2018, pp. 1991–1996, doi: 10.23919/IPEC.2018.8507912.

[14] M. Kaymak, R. W. D. Doncker, and T. Jimichi, "Design and verification of a medium-frequency transformer in a three-phase dual-active bridge DC-DC converter for medium-voltage grid connection of offshore wind farms," in *Proc. IEEE Appl. Power Electron. Conf. Expo. (APEC)*, 2020, pp. 2694–2701, doi: 10.1109/APEC39645.2020.9124482.

[15] M. Kharezy, H. R. Mirzaei, Y. Serdyuk, T. Thiringer, and M. Eslamian, "A novel oil-immersed medium frequency transformer for offshore HVDC wind farms," *IEEE Trans. Power Del.*, vol. 36, no. 5, pp. 3185–3195, Oct. 2021, doi: 10.1109/TPWRD.2020.3035718.

[16] Z. Guo, R. Yu, W. Xu, X. Feng, and A. Q. Huang, "Design and optimization of a 200-kW medium-frequency transformer for medium-voltage SiC PV inverters," *IEEE Trans. Power Electron.*, vol. 36, no. 9, pp. 10548–10560, Sep. 2021, doi: 10.1109/TPEL.2021.3059879.

[17] A. E. Shafei, S. Ozdemir, N. Altin, G. Jean-Pierre, and A. Nasiri, "Development of a medium voltage, high power, high frequency four-port solid state transformer," *CES Trans. Elect. Machines Syst.*, vol. 6, no. 1, pp. 95–104, 2022, doi: 10.30941/CESTEMS.2022.00013.

[18] Z. Yi, K. Sun, H. Liu, G. Cao, and S. Lu, "Design and optimization of the insulation of medium-voltage medium-frequency transformers for solid-state transformers," *IEEE Trans. Emerg. Sel. Topics Power Electron.*, vol. 10, no. 4, pp. 3561–3570, Aug. 2022, doi: 10.1109/JESTPE.2021.3094674.

[19] L. Zheng et al., "7.2 kV three-port SiC single-stage current-source solid-state transformer with 90 kV lightning protection," *IEEE Trans. Power Electron.*, vol. 37, no. 10, pp. 12080–12094, Oct. 2022, doi: 10.1109/TPEL.2022.3172946.

[20] W. Xu, Z. Guo, A. Vetrivelan, R. Yu, and A. Q. Huang, "Hardware design of a 13.8-kV/3-MVA PV plus storage solid-state transformer (PVS-SST)," *IEEE Trans. Emerg. Sel. Topics Power Electron.*, vol. 10, no. 4, pp. 3571–3586, Aug. 2022, doi: 10.1109/JESTPE.2021.3082033.

[21] A. Anurag, S. Acharya, S. Bhattacharya, T. R. Weatherford, and A. A. Parker, "A Gen3 10 kV SiC MOSFET-based medium-voltage three-phase dual active bridge converter enabling a mobile utility support equipment solid state transformer," *IEEE Trans. Emerg. Sel. Topics Power Electron.*, vol. 10, no. 2, pp. 1519–1536, Apr. 2022, doi: 10.1109/JESTPE.2021.3069810.

[22] M. Guillet et al., "Design and testing of a compact dry insulated medium frequency transformer prototype for medium voltage applications," in *Proc. PCIM Europe 2023; Int. Exhib. Conf. Power Electron., Intell. Motion, Renewable Energy Manage.*, 2023, pp. 1–10, doi: 10.30420/566091056.

[23] Z. Li, E. Hsieh, Q. Li, and F. C. Lee, "High-frequency transformer design with medium-voltage insulation for resonant converter in solid-state transformer," *IEEE Trans. Power Electron.*, vol. 38, no. 8, pp. 9917–9932, Aug. 2023, doi: 10.1109/TPEL.2023.3279030.

[24] L. Chen et al., "Investigation of SMEs-battery hybrid energy storage system for robustness enhancement of solid-state transformer," *IEEE Trans. Appl. Supercond.*, vol. 34, no. 8, Nov. 2024, Art no. 5500506, doi: 10.1109/TASC.2024.3463258.

[25] X. Ren, Y. Jiang, H. Weng, T. Long, and D. Xu, "Design and testing of a soft-switching solid-state transformer module," *IEEE Trans. Emerg. Sel. Topics Power Electron.*, vol. 12, no. 6, pp. 5977–5989, Dec. 2024, doi: 10.1109/JESTPE.2024.3447455.

[26] Z. Li, C. Zhao, Y. H. Hsieh, Q. Li, and F. C. Lee, "Partial fluctuation power control of resonant converter in solid-state transformer," *IEEE Trans. Ind. Electron.*, vol. 71, no. 10, pp. 12358–12367, Oct. 2024, doi: 10.1109/TIE.2023.3347828.

[27] International Electrotechnical Commission, Power transformers–Part 1: General, Std. IEC60076-1, 2011.

[28] International Electrotechnical Commission, "IEC 60270:2000 High-voltage test techniques–Partial discharge measurements," Int. Electrotechnical Commission, 2000. [Online]. Available: https://webstore.iec.ch/publication/5708

[29] IEEE Standard for Harmonic Control in Electric Power Systems, IEEE Std., Aug. 2022.

[30] R. Mirzadarani, Z. Li, Z. Qin, P. Vaessen, P. Bauer, and M. G. Niasar, "Current balancing technique for the high-current windings of medium-frequency transformers," *IEEE Trans. Ind. Electron.*, vol. 73, no. 3, pp. 4053–4063, Mar. 2026doi: 10.1109/TIE.2025.3618838.

[31] L. Bolzonella, R. Mirzadarani, and M. G. Niasar, "Medium frequency transformer optimization and insulation testing for solid state transformer applications," in *Proc. IECON 2025–51st Annu. Conf. IEEE Ind. Electron. Soc.*, 2025, pp. 1–6, doi: 10.1109/IECON58223.2025.11221021.

[32] E. S. Lee, J. H. Park, M. Y. Kim, and J. S. Lee, "High efficiency integrated transformer design in DAB converters for solid-state transformers," *IEEE Trans. Veh. Technol.*, vol. 71, no. 7, pp. 7147–7160, Jul. 2022, doi: 10.1109/TVT.2022.3168561.

[33] T. Yu et al., "Single-stage matrix-type solid-state transformer based on push–pull dab," *IEEE Trans. Power Electron.*, vol. 40, no. 1, pp. 2005–2016, Jan. 2025, doi: 10.1109/TPEL.2024.3464749.

[34] X. Zhang, Y. Xu, Y. Long, S. Xu, and A. Siddique, "Hybrid-frequency cascaded full-bridge solid-state transformer," *IEEE Access*, vol. 7, pp. 22118–22132, 2019.

[35] S. Meier, T. Kjellqvist, S. Norrga, and H. P. Nee, "Design considerations for medium-frequency power transformers in offshore wind farms," in *Proc. 13th Eur. Conf. Power Electron. Appl. (EPE)*, Barcelona, Spain, 2009, pp. 1–12.

[36] F. Nasirpour, T. Luo, M. G. Niasar, and M. Popov, "Multi-winding power transformer modeling for fast-front transients," *IEEE Trans. Power Del.*, vol. 40, no. 2, pp. 1054–1066, Apr. 2025, doi: 10.1109/TPWRD.2025.3535419.

[37] ThyssenKrupp Electrical Steel GmbH. Grain Oriented Electrical Steel powercore – Product Range, 2020. Accessed: Jul. 2025. [Online]. Available: https://www.thyssenkrupp-steel.com

[38] ThyssenKrupp Electrical Steel GmbH. Non Grain Oriented Electrical Steel PowerCore#math#2, 2010. Accessed: Jul. 2025. [Online]. Available: https://www.thyssenkrupp-steel.com

[39] *International Electrotechnical Commission, IEC 60076-3: Power Transformers–Part 3: Insulation Levels, Dielectric Tests and External Clearances in Air*, Standard, iEC 60076-3:2018, 2018.

REZA MIRZADARANI (Graduate Student Member, IEEE) was born in Isfahan, Iran, in 1991. He received the M.Sc. degree in power systems from the University of Kashan, Kashan, Iran, in 2018.

He has worked on various high-voltage power electronics projects and joined the Delft University of Technology (TU Delft) as a Ph.D. candidate to focus on the design of medium-voltage, medium-frequency transformers for solid-state transformers in green hydrogen production. His current research interests include medium-frequency transformers, partial discharge mitigation, and medium-frequency, medium-voltage testing techniques.

Mr. Mirzadarani was the recipient of IEEE International Challenge in Design Methods for Power Electronics Excellent Innovation Award 2023.

LEONARDO BOLZONELLA (Student Member, IEEE) was born in Latisana, Italy, in 2000. He received the B.Sc. degree in electrical engineering from the University of Twente, Twente, The Netherlands, in 2022, and the M.Sc. degree, specializing in power electronics and high voltage, from the Delft University of Technology, Delft, The Netherlands, in 2025. He iscurrently working toward the Ph.D. degree in metrology for very fast transient overvoltages with TU Delft, Delft.

His research interests include metrological techniques, nanosecond pulse generation, medium-frequency transformers and high-voltage testing.

ZHENGZHAO LI (Student Member, IEEE) received the B.Sc. degree in electrical engineering from Tongji University, Shanghai, China, in 2018, and the M.Sc. degree in electrical engineering from Shanghai Jiao Tong University, Shanghai, in 2021. He is currently working toward the Ph.D. degree in electrical engineering with the Delft University of Technology, Delft, The Netherlands.

His research focuses on the design and modeling of solid-state transformers.

ZIAN QIN (Senior Member) received the B.Sc. degree in electrical engineering from Beihang University, Beijing, China, in 2009, the M.Sc. degree in electrical engineering from the Beijing Institute of Technology, Beijing, China, in 2012, and the Ph.D. degree in electrical engineering from Aalborg University, Aalborg, Denmark, in 2015.

In 2014, he was a Visiting Scientist with RWTH Aachen University, Aachen, Germany. He is currently an Associate Professor with the Department of Electrical Sustainable Energy, Delft University of Technology, Delft, The Netherlands. He has authored more than 100 journal and conference papers, four book chapters, and several international patents, and has led or contributed to numerous European, Dutch national, and industrial projects. He has also delivered more than ten invited tutorials and keynote talks at international conferences and industry events. His research interests include power quality and stability of power electronics-based grids, solid-state transformers, and battery energy storage.

Dr. Qin has held leading roles in major conferences, including Technical Program Chair for IEEE-PEDG 2024, IEEE-PEDG 2023, IEEE-ISIE 2020, and IEEE-COMPEL 2020. He was the recipient of the IEEE Open Journal of Power Electronics Prize Paper Award (2020–2023) and the IEEE International Challenge on Design Methods for Power Electronics Excellent Innovation Award (2023).

PETER VAESSEN (Member, IEEE) received the M.Sc. degree (cum laude) in electrical power engineering from Eindhoven Technical University, Eindhoven, The Netherlands, in 1985.

In 1985, he joined KEMA (now a CESI brand). In his 40-year career, he held the research positions in the field of large power transformers and high-voltage measurement and testing. He headed Transmission and Distribution High Voltage Department and managed realization projects, among them the construction of Dutch 400 kV substations and laboratory test facilities. As a Principal Consultant, he has 25 years of experience in (U)HVDC technology and transmission and distribution grids with high shares of renewables. He is the Manager of innovations with CESI and is actively involved in the technology strategy. He is the Chairman of the Board of the European Distributed Energy Resources Laboratories Association and a Member of several national and international working groups. He is a part-time Professor of hybrid transmission systems with the Delft University of Technology, Delft, The Netherlands, where he teaches high-voltage technology and HVDC.

PAVOL BAUER (Senior Member, IEEE) received the master's degree in electrical engineering from the Technical University of Kosice, Kosice, Slovakia, in 1985, and the Ph.D. degree in electrical engineering from the Delft University of Technology, Delft, The Netherlands, in 1995.

From 2002 to 2003, he was with KEMA (DNV GL), Arnhem, The Netherlands, on different projects related to power electronics applications in power systems. He is currently a Full Professor with the Department of Electrical Sustainable Energy, Delft University of Technology, and the Head of DC Systems, Energy Conversion, and Storage Group. He is also a Professor with the Brno University of Technology, Brno, Czech Republic, and an Honorary Professor with the Politehnica University Timisoara, Timisoara, Romania. He is an author or coauthor of eight books, holds seven international patents, and organized several tutorials at international conferences.

Prof. Bauer is the Former Chairman of Benelux IEEE Joint Industry Applications Society, Power Electronics and Power Engineering Society Chapter, the Chairman of the Power Electronics and Motion Control Council, a Member of the Executive Committee of European Power Electronics Association, and also a Member of the International Steering Committee at numerous conferences.

MOHAMAD GHAFFARIAN NIASAR (Member, IEEE) was born in Tehran, Iran, in 1984. He received the M.Sc. degree in electrical power engineering from the Sharif University of Technology, Tehran, Iran, in 2008, and the Ph.D. degree in electrical engineering from the Royal Institute of Technology, Stockholm, Sweden, in 2015.

He is currently an Associate Professor with High Voltage Technologies Group, Delft University of Technology, Delft, The Netherlands. His research interests include the aging of electrical insulation, HVDC insulation system, partial discharges, high-frequency power transformers, power cables, and FEM modeling.